The FEBS Journal

FEBS PRESS
science publishing by scientists

Interaction mechanism of endogenous PP2A inhibitor protein ENSA with PP2A

Chandan Thapa[1,2,3], Pekka Roivas[2,3], Tatu Haataja[1], Perttu Permi[1,4] and Ulla Pentikäinen[2,3]

1 Department of Biological and Environmental Science and Nanoscience Center, University of Jyvaskyla, Finland
2 Institute of Biomedicine, University of Turku, Finland
3 Turku BioScience, University of Turku, Finland
4 Department of Chemistry and Nanoscience Center, University of Jyvaskyla, Finland

Keywords

ENSA; IDPs; NMR; PP2A; PP2A inhibitor protein; SAXS

Correspondence

P. Permi, Department of Biological and Environmental Science and Nanoscience Center, University of Jyvaskyla, 40014 Jyvaskyla, Finland
Tel: +35 840 8054288
E-mail: perttu.permi@jyu.fi
U. Pentikäinen, Institute of Biomedicine, University of Turku, 20520 Turku, Finland
Tel: +35 850 5012574
E-mail: ulla.pentikainen@utu.fi

(Received 29 April 2021, revised 6 July 2021, accepted 3 August 2021)

doi:10.1111/febs.16150

The vast diversity of protein phosphatase 2A (PP2A) holoenzyme composition ensures its multifaceted role in the regulation of cellular growth and signal transduction. In several pathological conditions, such as cancer, PP2A is inhibited by endogenous inhibitor proteins. Several PP2A inhibitor proteins have been identified, one of which is α-endosulfine (ENSA). ENSA inhibits PP2A activity when it is phosphorylated at Ser67 by Greatwall (Gwl) kinase. The role of ENSA in PP2A inhibition is rather well characterized, but knowledge of the mechanism of inhibition is scarce. In this study, we have performed comprehensive structural characterization of ENSA, and its interaction with PP2A A- and various B56-subunit isoforms by combining NMR spectroscopy, small-angle X-ray scattering (SAXS) and interaction assays. The results clearly indicate that ENSA is an intrinsically disordered protein containing three transient α-helical structures. ENSA was observed to interact PP2A mainly via A-subunit, as the affinity with the A-subunit is significantly stronger than with any of the B56 subunits. Based on our results, it seems that ENSA follows the dock-and-coalesce mechanism in associating with PP2A A-subunit. Taken together, our results provide an essential structural and molecular framework to understanding molecular bases of ENSA-mediated PP2A inhibition, which is crucial for the development of new therapies for diseases linked to PP2A inhibition.

Introduction

Human α-endosulfine belongs to endosulfine family and is closely related to cAMP-regulated phosphoprotein-19 (ARPP-19) but encoded by distinct genes [1]. ENSA is expressed in broad spectrum of tissues suggesting its role in multiple physiological processes. The expression level of ENSA is high in muscles and brain and low in pancreas [2], resembling tissue distribution of ATP-sensitive potassium channel (K-ATP) channel [3–5], and initially ENSA was identified as an endogenous ligand regulating the ATP-dependent potassium channel [6]. *In vitro* studies have shown that ENSA regulates the secretion of insulin by interacting with K-ATP channels [2]. It has been reported that the ENSA modulates the release of

Abbreviations

ARPP, cAMP-regulated phosphoprotein; CSP, chemical shift perturbation; ENSA, α-endosulfine; EOM, ensemble optimization method; Gwl, greatwall kinase; IDP, intrinsically disordered proteins; K-ATP, ATP-sensitive potassium channel; MAST3, microtubule-associated serine/threonine kinase 3; MASTL, microtubule-associated serine/threonine like kinase; MST, microscale thermophoreis; NOE, nuclear overhauser effect; PP2A, protein phosphatase 2A; R_1, longitudinal relaxation rate; R_2, transverse relaxation rate; SAXS, small-angle X-ray scattering; SSP, secondary structure propensity.

neurotransmitter, acetylcholine, by blocking K-ATP channels [7]. The expression of human ENSA in brain is decreased in Down syndrome [8], Alzheimer's disease [3] and synucleinopathies [9].

α-endosulfine also acts as both a substrate and an inhibitor of PP2A [10]. PP2A is a major serine/threonine phosphatase, which is crucial for many normal cellular functions, such as cell cycle control, growth, apoptosis and metabolism. Therefore, it is not surprising that its dysregulation is observed in many pathological conditions, for example in cancer and neurodegenerative diseases [11]. Several proteins, such as CIP2A [12], SET [13], ARPP-19 [14,15] and ENSA [15], have been observed to act as PP2A inhibitors. PP2A is a heterotrimeric protein complex consisting of a scaffold (called A-subunit), a catalytic (called C-subunit) and a regulatory (called B-subunit) subunits. Each of the subunits has multiple isoforms. The subunits A and C have two structurally similar isoforms, whereas the B-subunit has 23 isoforms that are divided into four different families (such as B55, B56, PR72 and Straitins), each of these having various subtypes (such as B56α, B56δ, B56ε and B56γ). The B-subunits have more structural variation than the A- and C-subunits (Fig. 1). Accordingly, the assembly of one A-subunit, one C-subunit and one B-subunit can give 92 different heterotrimers [16]. Even though the functions of different B-subunits are partly redundant, the localization, specificity and physiological activity of PP2A largely depend on the type of B-subunit associated with the holoenzyme. This broad diversity in the PP2A composition allows PP2A to act on large number of substrates and influence on many cellular processes including cell cycle apoptosis and transformation [17]. It has also been reported that the overexpression of ENSA suppresses hepatic tumour growth when phosphorylated by the MASTL kinase [18].

Both ENSA and PP2A play a critical role in cell cycle control. Both mitotic entry and exit are controlled by phosphorylation/dephosphorylation of mitotic proteins, which is achieved by the balanced activities kinases and phosphatases. The mitotic entry requires the activation of cycling B-Cdc2 protein kinase that phosphorylates the mitotic proteins, and the maintenance of the phosphorylation of mitotic proteins requires the inhibition of PP2A that dephosphorylates mitotic substrates. ENSA, which is phosphorylated by greatwall kinase/microtubule-associated serine/threonine like kinase/microtubule-associated serine/threonine kinase 3 (Gwl/MASTL/MAST3) kinase, inhibits the activity of PP2A containing B55δ regulatory subunit, allowing then the mitotic entry [14,15,19].

Owing to the enormous diversity of PP2A regulatory subunit and its redundant cellular function, the study of regulation of individual regulatory subunit is important. In this study, we have characterized the structural properties of PP2A inhibitor protein ENSA using NMR spectroscopy and SAXS. Structural analyses reveal that ENSA is an IDP containing three transient alpha helical regions. In addition to structural characterization, we investigated the mechanism how ENSA interacts with PP2A. Firstly, we observed that ENSA interacts with the PP2A A-subunit with moderately strong affinity, but it also interacts with various B56-subunit isoforms, although the affinity to B56 is much weaker. The combination of interaction studies performed with the microscale thermophoresis (MST) and NMR spectroscopy reveals that ENSA follows the dock-and-coalesce mechanism in associating with the PP2A A-subunit.

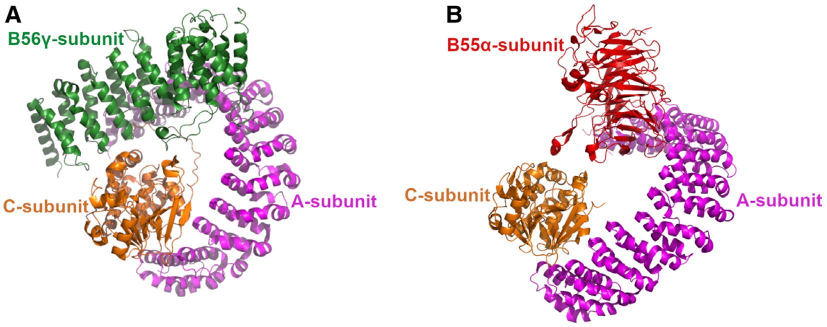

Fig. 1. The 3D structure of PP2A holoenzyme. (A) The scaffolding A-subunit (PR65α) is shown with magenta, regulatory B56γ subunit shown with green and the catalytic Cα-subunit with orange. The coordinates are taken from 2 npp.pdb. (B) The scaffolding A-subunit (PR65α) is shown with magenta, regulatory B55α subunit shown with red and the catalytic Cα-subunit with orange. The coordinates are taken from 3dw8.pdb. The structure is generated using PYMOL (http://www.pymol.org) software.

Results and Discussion

Characterization of local conformational properties of ENSA

First, we performed the sequence analysis of ENSA, which shows the enrichment of the hydrophilic (25%) and charged (33%) amino acid residues as well as prolines (7.4%), similarly as ARPP-19 (Fig. 2A). These are fundamental features of IDPs [20,21]. According to Uversky plot [22], which divides proteins into globular and IDPs based on their mean net charge versus hydropathy, ENSA locates within natively disordered protein space (Fig. 2B). The PONDR® VL-XT algorithm [23] was used to predict the disordered regions of ENSA. This indicated that 56% of residues are in disordered regions in ENSA (Fig. 2C). We also used IUPred2A, an unified platform that uses IUPred2 and ANCHOR2 algorithms, to obtain more information about the level of disorder and the potential binding regions [24,25]. The IUPred2 tool predicted ENSA to be fully disordered, whereas the ANCHOR2 tool predicted the presence of single extended disordered binding region ranging from residues K24-E121 (Fig. 2C). Both, PONDR VL-XT and IUPred2A, tools predicted that the N and C termini of ENSA are disordered and the core region being relatively ordered. However, the prediction with PONDR VL-XT showed the higher degree of order for the core region than the IUPRED2A-based prediction. The degree of order predicted for the core region deviates between these two methods because they are based on different principles and apply different computational approach.

We employed NMR spectroscopy to further study the structural features of ENSA. Two-dimensional ^{1}H ^{15}N-HSQC spectrum of ENSA exhibits poorly dispersed $^{1}H^{N}$ cross peaks, ranging from 7.7 to 8.5 p.p.m., originating from strikingly similar chemical environment of amide protons due to fast conformational averaging (Fig. 2D). The SAXS scattering profile of ENSA corresponds to that of IDPs obtained after averaging curves for a large number of interconverting conformers (Fig. 3A). In addition, the distance distribution function $p(r)$ of ENSA has an extended tail indicating the flexible nature of ENSA (Fig. 3B; Table 1). The Kratky analyses of SAXS data also supported the disordered nature of ENSA because it presented a monotonic Kratky plot at large s values (Fig. 3C). Accordingly, the structural properties of ENSA are highly similar to their close homologue, ARPP-19 [26,27].

The ^{1}HN, ^{1}Hα, ^{15}N, ^{13}CO, ^{13}Cα and ^{13}Cβ resonance assignment was carried out using 2D ^{15}N-HSQC [28], ^{13}C-detected CON [29] and 3D CBCA(CO)NH, HNCACB [30], HNCO [31], iHNCO, iHA(CA)NCO, HA(CA)CON and (HACA)CON(CA)HA [32–34] spectra. The chemical shift values contain wealth of information about transient secondary structure motifs. The transient secondary structure elements were identified by calculating secondary structure propensity (SSP) score [35], using ^{1}Hα, ^{13}Cα and ^{13}Cβ chemical shift values. The SSP analysis revealed the presence of three transient alpha helical regions (Fig. 2C). Comparing the result obtained from SSP calculation of ENSA and ARPP-19 [27], we found that the transient helices in both proteins are located at the corresponding positions and their distribution patterns are also similar.

Further evidence of the presence of secondary structure elements was obtained from T_1 and T_2 ^{15}N spin relaxation and heteronuclear {^{1}H}^{15}N nuclear overhauser effect (NOE) NMR experiments (Fig. 4A), which are the reporters of the ps-ns backbone dynamics. We adapted reduced spectral density mapping [36,37] approach to comprehend ^{15}N relaxation data of ENSA. The calculated reduced spectral densities $J(0)$, $J(\omega_N)$ *and* $J(0.87\ \omega_H)$ explain the dynamics of residues at three different frequency (Fig. 4B). The low-frequency spectral density $J(0)$ has smaller value for the residues with fast internal motion, while residues with slow internal motion tend to have significantly higher values. The high-frequency spectral density $J(0.87\omega_H)$ is sensitive to fast internal motions, and motions are reflected in relatively large values. Therefore, the residues in secondary structure elements show large $J(0)$ and small $J(0.87\omega_H)$ values, indicating the restricted internal motion. The overall distribution of reduced spectral densities $J(0)$ *and* $J(0.87\ \omega_H)$ suggests that the backbone motion in the regions encompassing residues ^{31}RAEEAKLKAK^{40} and ^{53}FLMKRLQKGQKYFDSGDYNMAKAKMKN^{79} is restricted. However, residues N71 and M72 have higher $J(0)$ values, but $J(0.87\ \omega_H)$ did not decrease significantly suggesting restricted internal motions or conformational exchange at lower frequency. The N and C termini of ENSA are flexible in nature, as indicated by relatively large value of $J(0.87\ \omega_H)$. The values of spectral density function $J(\omega_N)$ are relatively invariable, indicating its insensitivity towards backbone dynamics (Fig. 4B). The regions with restricted backbone motions are present in the similar locations in both ENSA and ARPP-19. The result clearly shows two regions with the restricted backbone dynamics in both ARPP-19 and ENSA, but the second region with restricted motion is wider in ENSA than that of ARPP-19 [27].

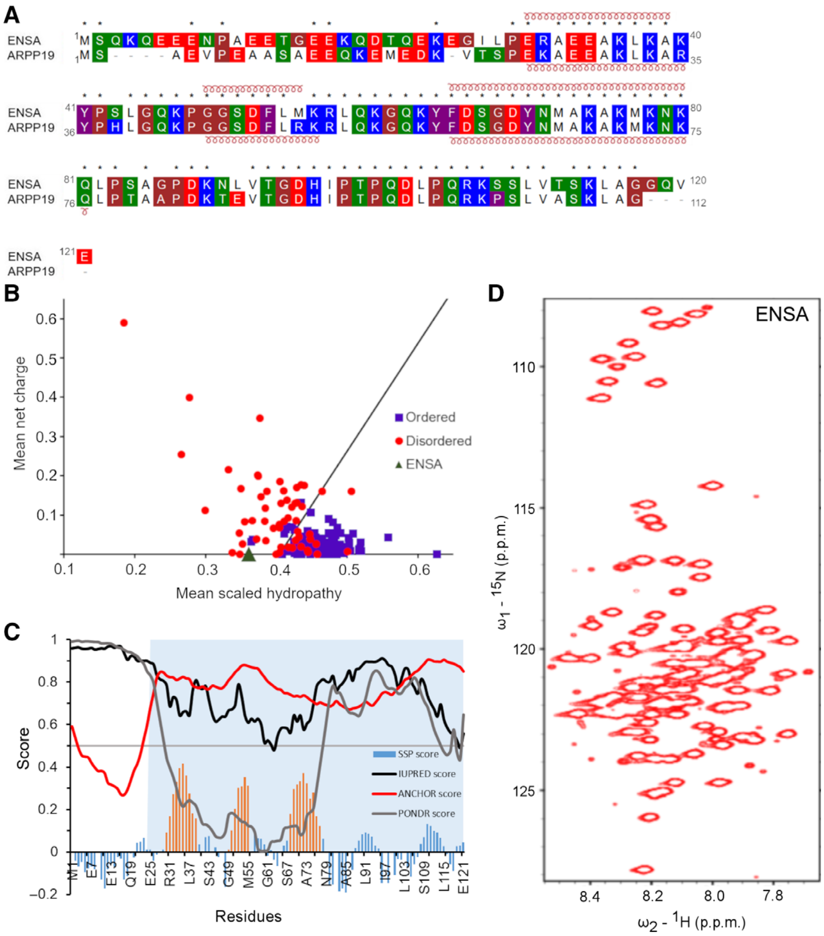

Fig. 2. α-endosulfine is IDP having propensity to form transient structural elements. (A) Pairwise sequence alignment between human ENSA and ARPP-19. The amino acids are highlighted with different colours according to their properties like the positively charged residues (blue), negatively charged residues (red), polar neutral residues (green), aromatic residues (purple) and conformationally special proline and glycine residues (brown). The nonpolar aliphatic residues are not highlighted. The secondary structure elements obtained from SSP calculation for ENSA and ARPP-19 is shown in the figure. (B) Charge-hydropathy plot of human ENSA. The mean net charge versus the mean hydrophobicity plot (calculated at http://www.pondr.com) predicts ENSA (green triangle) to be disordered. (C) PONDR VL-XT, IUPred2A analysis and SSP calculation of ENSA. The output of PONDR VL-XT, IUPred2 and ANCHOR2 for the ENSA are shown in grey, black and red, respectively. The SSP score for ENSA was calculated using ^{1}Hα, ^{13}Cα and ^{13}Cβ chemical shifts. The SSP score of residues with fully formed α-helices and β-strands are +1 and −1, respectively. It indicates that ENSA has propensity to form three transient α-helices. The positions of α-helices are highlighted with orange colour. (D) Two-dimensional ^{1}H, ^{15}N-HSQC spectra of uniformly ^{15}N-labelled ENSA corresponds to the spectral overlap in IDPs.

Structural characterization of ENSA in solution

Intrinsically disordered proteins lack a well-defined three-dimensional structure, unlike the ordered proteins. Therefore, it is not possible to show one single structure for ENSA but an ensemble of different conformations instead. Here, we combined the restraints obtained from NMR experiments, such as chemical shifts (Cα, Cβ, HN) and ^{15}N R_2 relaxation rates, with the distance distribution data obtained SAXS measurements. The agreement between experimental and back-calculated SAXS scattering profile and the secondary NMR chemical shifts are shown in Fig. 5. The pool of structures shows that ENSA can adopt a continuum of rapidly interconverting conformers of which some are more compact than others (Figs 6 and 7). The conformers of ENSA obtained from the ENSEMBLE calculation were clustered according to the CαCα distance matrix RMSDs using NMRCLUST algorithm [38]. The NMRCLUST clustered 100 conformers of ENSA into 20 different subclusters. The top six clusters of ENSA have 15, 10, 10, 15, 7 and 8 conformers each, while rest of the clusters are composed of 1–5

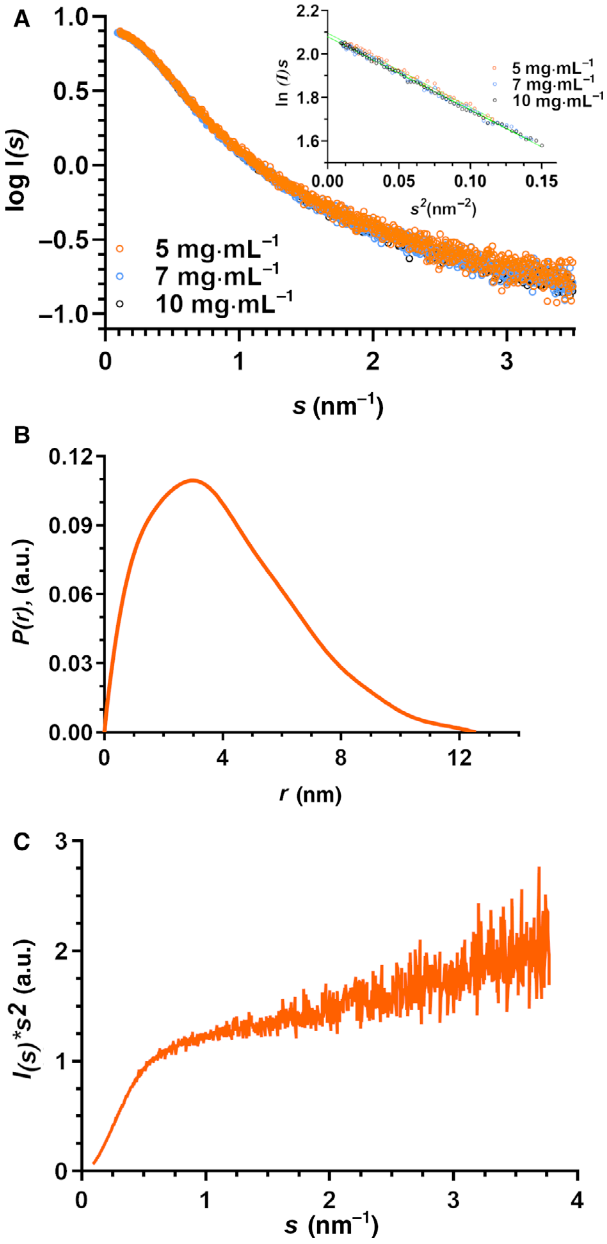

Fig. 3. (A) Small-angle X-ray scattering profiles with the inset showing the Guinier fits of the ENSA protein at 5, 7 and 10 mg·mL^{-1} concentrations. (B) Pairwise distance distribution, *P(r)*, estimation derived from SAXS data. (C) The Kratky plot calculated from SAXS data obtained at 7 mg·mL^{-1} concentration of ENSA exhibits monotonic Kratky plot at larger *s* values corresponding to the scattering pattern of IDPs.

Table. 1. SAXS data processing of ENSA.

	ENSA		
	5 mg·mL^{-1}	7 mg·mL^{-1}	10 mg·mL^{-1}
Guinier analysis			
I(0; arbitrary units)	8.14 ± 0.03	8.01 ± 0.02	7.99 ± 0.02
R_g (nm)[a]	3.21 ± 0.03	3.18 ± 0.02	3.18 ± 0.01
s_{min} (nm^{-1})	0.367	0.319	0.305
sR_g max (nm^{-1})	1.09	1.2	1.23
Coefficient of correlation, R^2	0.99	0.995	0.997
P(r) analysis			
I(0; arbitrary units)	5.1 ± 0.02	5.2 ± 0.02	5.4 ± 0.02
R_g (nm)	2.9 ± 0.02	2.9 ± 0.02	3.03 ± 0.02
D_{max} (nm)[b]	10.7	11.2	11.85
s range (nm^{-1})	0.124–2.824	0.138–2.889	0.129–2.810
X^2 (total estimate from GNOM)	0.95 (0.79)	0.98 (0.78)	0.87 (0.75)

[a]Estimated from Guinier analysis in PRIMUS [43].; [b]Calculated using DATGNOM [44].

conformers. The average CαCα RMSD of the ENSA clusters is high, ranging from 15 to 21 Å, demonstrating notable conformational difference among the population of conformers within the cluster (Fig. 6; Table 2). This is in agreement with the distance distribution calculated from using ensemble optimization method (EOM) analyses of the SAXS data, which shows a wide distribution of maximum distances ranging from 5 to 16 nm (Fig. 7; Table 3). This is different from what was recently reported for ARPP-19, where two distinct conformational populations, compact and more extended, were observed [27].

α-endosulfine-PP2A interaction

The binding affinity of ENSA and its phosphomimicking mutants S67E and S109E to PP2A A- and different B56-subunits was characterized using MST. ENSA and its phosphomimicking mutants bind relatively tightly to the PP2A A-subunit with dissociation constants (K_D) of 3.9 ± 1.3 μM (ENSA), 2.5 ± 1.1 μM (ENSA S67E) and 10.8 ± 3.2 μM (ENSA S109E; Fig. 8; Table 4). The binding affinity of ENSA-PP2A A-subunit complex is comparable to the ARPP-PP2A A-subunit interaction [27]. This is the outcome of high sequence similarity between ENSA and ARPPs. The region in ARPPs that binds to the A-subunit, ^{39}LGQKPGGSDFLRKRLQKGQKYFDS^{62}, is highly conserved in ENSA with only one change in amino acid, that is Met instead of Arg50 in ARPP-19.

We also determined the interaction of ENSA and its phosphomimicking mutants with four different B56 isoforms, B56α, B56δ, B56γ and B56ε (Fig. 8; Table 4). ENSA binds to all B56 isoforms, but the

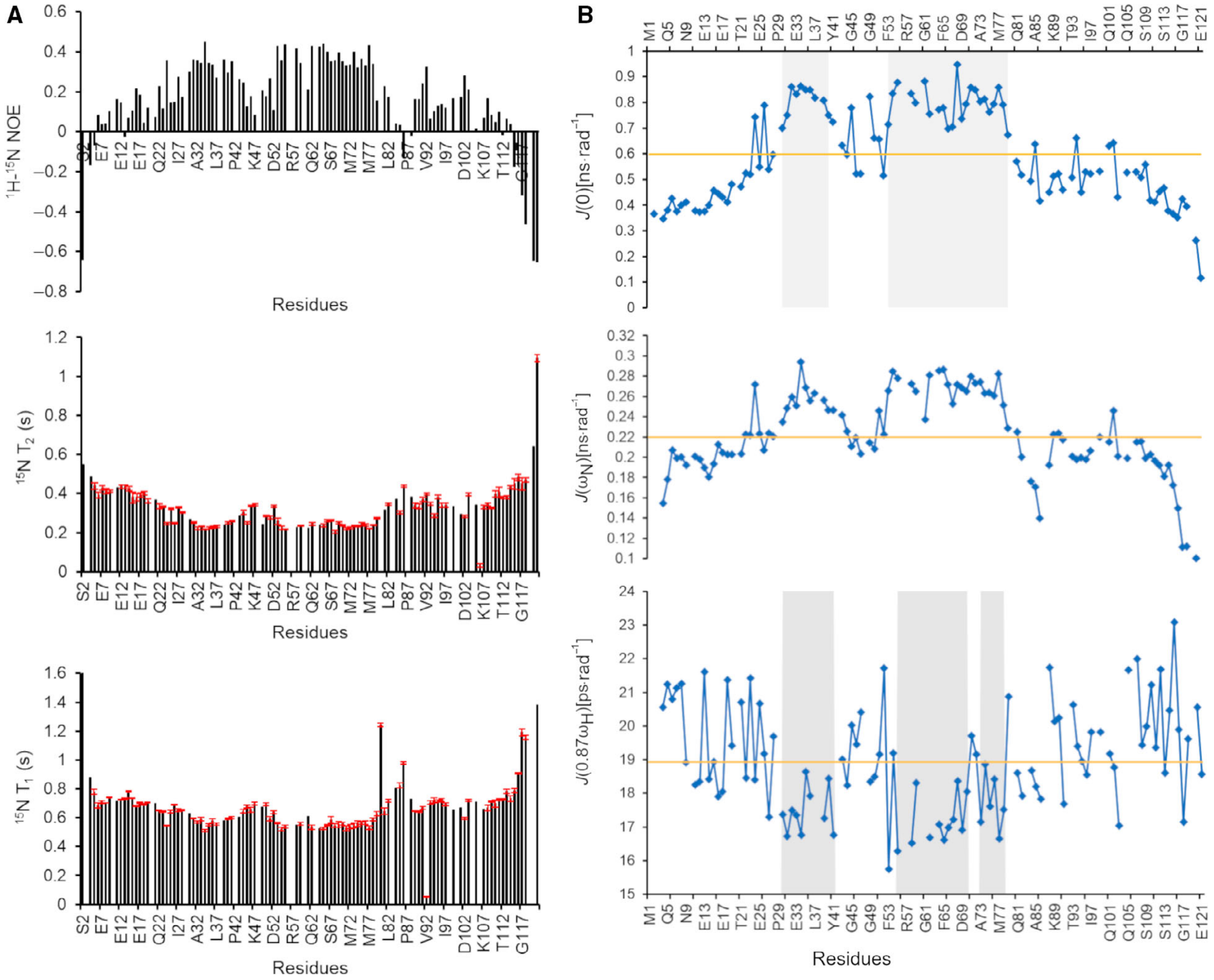

Fig. 4. Nuclear magnetic spectroscopy relaxation data indicate the conformational dynamics in the disordered ENSA. (A) Values of backbone amide heteronuclear {^{1}H}-^{15}N NOEs, transverse relaxation (^{15}N T$_2$) and longitudinal relaxation (^{15}N T$_1$) of the ENSA obtained at 800 MHz at 25 °C. (B) Reduced spectral density mapping function calculated at three different frequencies, *J(0), J(ω$_N$) and J(0.87ω$_H$)* is plotted against the sequence of ENSA. Transiently formed α-helical regions are highlighted.

interaction is clearly weaker than to A-subunit. Strongest binding was observed with B56α, while the affinities to all other B56 isoforms are very weak. This is similar to the binding recently observed with ARPP-19. [27] According to the calculated K_D values, the binding of ENSA to B56 isoforms is stronger than the interaction between ARPP-19 and B56 isoforms. [27] Interestingly, it has been reported that ENSA does not bind to any other PP2A than those containing B55 as a regulatory subunit suggesting that ENSA is specific only for PP2A-B55. [15] The contradiction in the results might be due to different experimental set-ups, as here we have used individual PP2A subunits and not PP2A holoenzyme, as our aim was to get information of ENSA – individual PP2A subunit interactions. Unfortunately, we did not have any of B55 isoforms in our hands. Surprisingly, ENSA S67E, which corresponds to the Gwl/MAST3 kinase phosphorylated ENSA, binds only to the B56α, but not to other isoforms (Table 4). The measured binding affinities of ENSA and S67E phosphomimicking mutant to B56α are similar.

We further applied NMR spectroscopy to characterize the interaction between ENSA and the A-subunit. The interaction of ^{15}N-labelled ENSA with the A-subunit was confirmed by monitoring overall peak dispersion in ^{15}N-HSQC spectra after addition of the A-subunit. Accordingly, we observed PP2A A-subunit binding induced changes in the ^{15}N-HSQC spectra of ENSA indicating changes in the average chemical environment of the corresponding residues (Fig. 9A–C). At the same time, no pronounced change in chemical

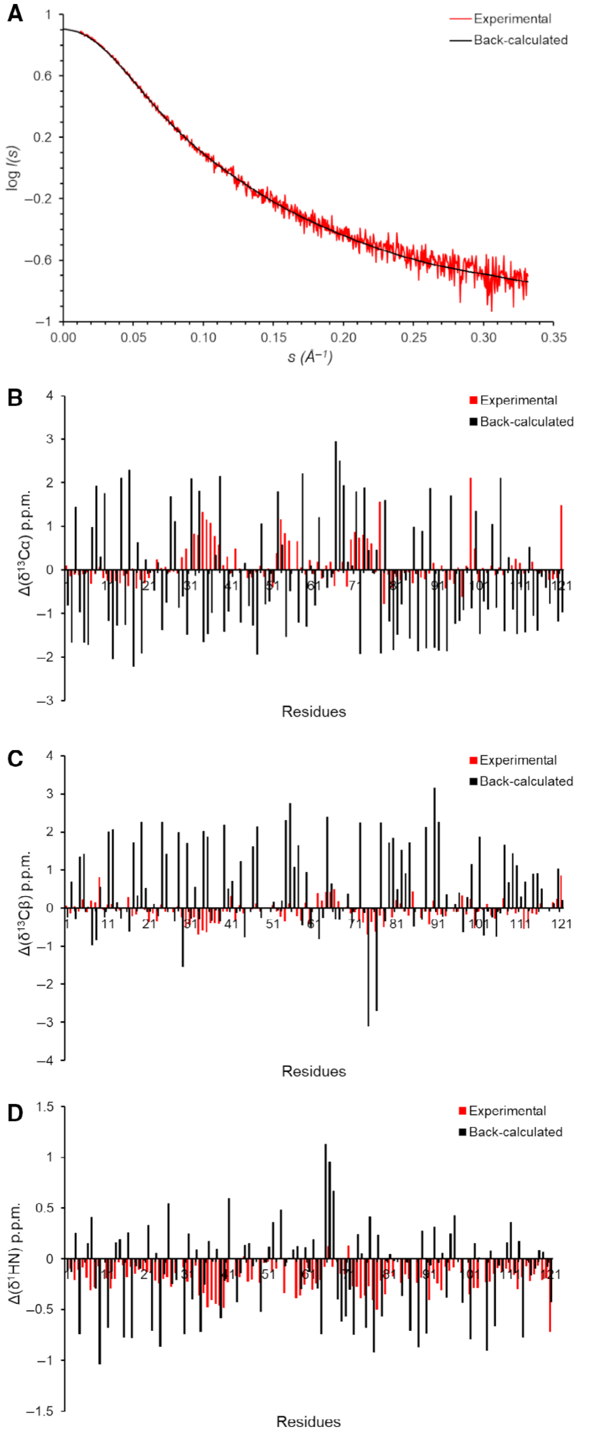

Fig. 5. The fitting of SAXS and NMR experimental and back-calculated data: (A) Averaged back-calculated SAXS intensities derived from an ensemble of 100 conformers (black) compared with the experimental data of ENSA (red) using CRYSOL [48] program in ATSAS online. (B–D) The comparison of secondary chemical shifts of the experimental NMR chemical shifts (^{13}Cα, ^{13}Cβ and ^{1}HN) and the one back-calculated using ShiftX [54] program.

shift dispersion of ENSA was observed upon the A-subunit binding. This suggests that no large-scale disorder to order transition takes place upon binding, that is ENSA undergoes local binding-induced folding, governed by the molecular recognition elements in the sequence (Fig. 9A–C). However, it seems that partial coupled folding takes place upon binding to A-subunit, ENSA retains high degree of flexibility even in the bound state and this highly dynamic PP2A A-subunit: ENSA complex is an evident example of the ‘fuzzy complex’ concept [39]. Owing to large size of the complex, as well as the additional exchange broadening of NH resonances due to the intermediate exchange limit typical for the interactions with K_D of 5–10 µM, we could not detect all the ^{15}N-^{1}H correlation of ENSA in the bound form. Nevertheless, a more profound analysis of ENSA–PP2A A-subunit binding enabled us to propose binding mechanism for the interaction (*vide infra*).

A detailed view of the PP2A A-subunit binding site in ENSA was obtained by monitoring PP2A A-subunit-induced chemical shift perturbations (CSPs) in ^{15}N-HSQC spectra of ENSA (Fig. 9A–C). Upon addition of PP2A A-subunit at the concentration half of the molar concentration of ENSA, significant CSPs were observed for the NH cross peaks of following residues: A35, A39, M55, Y64, D66 and N71. The residues L54 and F65 experienced line broadening beyond the NMR detection limit (Fig. 9A). After adding equimolar concentration of PP2A A-subunit to ENSA (molar ratio of 1 : 1), we observed additional CSPs together with significant line broadening for the following ENSA NH cross peaks: R31, K36, L37, K40, Y41, Q59, G68 and M72. In addition to this, NH cross peaks of A35, F53, L54, M55, Q62, F65, S67, N71 and A75 were broadened beyond detection (Fig. 9B). When the A-subunit concentration was increased to the molar ratio 1 : 2 (ENSA:A-subunit), the NH cross peaks of S43, S51, G61, D69 and K76 were significantly broadened and the peak from G68 broadened beyond detection (Fig. 9C) The close examination of ENSA ^{15}N-HSQC spectra without the A-subunit and the spectra with substoichiometric ENSA: PP2A A-subunit (1 : 0.5) ratio and one- or twofold excess of A-subunit revealed peak shift or strong line broadening of the cross peaks corresponding to the residues A30-G45 (binding site B1) and S51-K76 (binding site B2). Based on the result reported here, ENSA binding to PP2A A-subunit consist of extended region comprising all three transiently populated helices (Fig. 9D) and is in good agreement with the disordered binding region predicted by ANCHOR2 (Fig. 2C). Accordingly, the binding of PP2A to ENSA

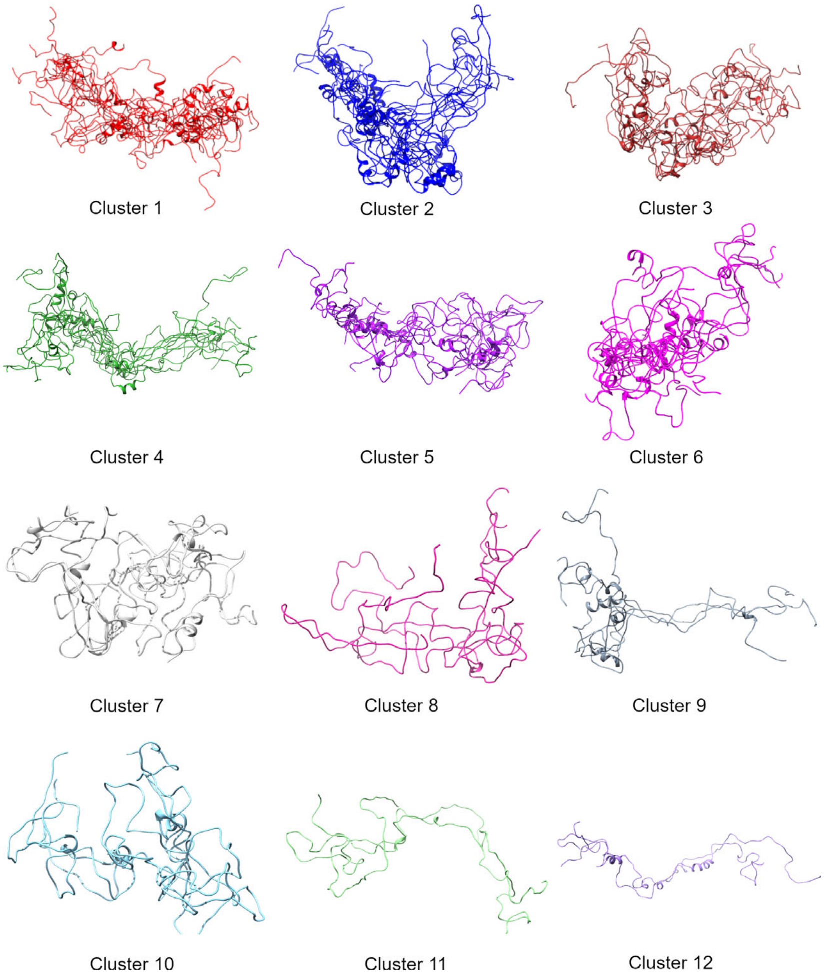

Fig. 6. Cluster of substrates in the ensemble of ENSA as determined by NMR and SAXS experiments. The top 12 clusters of the representative NMR structure of the total 100 structures are shown. The structures are generated using UCSF ChimeraX [55].

is a complex process that may use transient interaction with α-helical peptide region that function as the molecular recognition elements. From the consideration of CSPs, this is what we would expect: the ENSA will initially interact with PP2A A-subunit using the B2 region (primary site), as it is seen from the line broadening beyond detection of the ENSA NH cross peaks for the residues L54 and F65 measured at 1:0.5 (ENSA:PP2A A-subunit) ratio. After adding more PP2A, we can see that ENSA interacts with the PP2A A-subunit with the additional secondary site (B1; Fig. 10). Alternatively, helices undergo partial folding upon PP2A binding, establishing intramolecular interactions between helices. It is possible that the observed peak shifts and line broadening are the consequence of conformational dynamics and increase in the effective rotational correlation time upon PP2A A-subunit binding. This is different than that recently reported with ARPP-19, where the A-subunit binding region is mapped between first and third helices including the second transient alpha helix and random coil region on its both sides. [27] Accordingly, it can be speculated that ENSA binds to the A-subunit using different interaction modes than that of ARPP proteins. This is surprising, as ENSA and ARPP-19 share 76% sequence identity. However, the N-terminal sequences in ENSA and ARPP-19 are very different (Fig. 2A). Although we observed very tiny CSPs in few residues of the first helix of ARPP-19 upon titration by PP2A A-subunit, they were not as large and significant as we observed in ENSA. The small changes that was observed in ARPP-19 can be due to a very transient interaction or due to the influence of changes in chemical environment in the vicinity. In general, the secondary binding site B1 in ENSA interacts more transiently with the PP2A A-subunit and the CSPs were observed only after titrating equimolar concentration of PP2A A-subunit. Nevertheless, this interaction appears to be enforced by the negatively charged N-terminal part in ENSA.

In summary, here we have reported the detailed analysis of the structural and dynamical features of

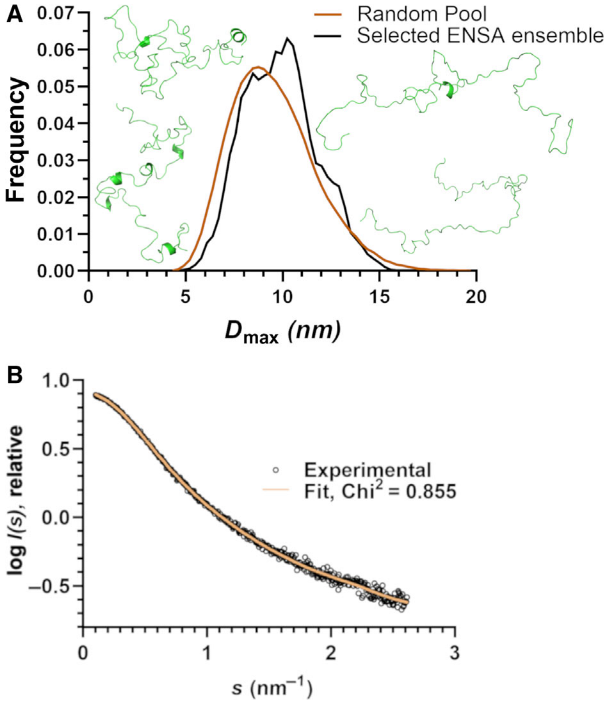

Fig. 7. α-endosulfine can adopt broad ensemble of conformations. (A) The comparison of D_{max} distribution of the EOM selected conformational ensemble of ENSA obtained from the SAXS measurement (shown in black) with the initial theoretical pool based only on the amino acid sequence information (shown in red). Cartoon representation of a few ENSEMBLE generated conformers of ENSA that fits the chemical shifts (Cα, Cβ, H), R_2 relaxation rates from NMR spectroscopy and the SAXS scattering data. (B) The fit obtained from the selected ensemble of structures in EOM calculations to experimental scattering curve.

Table. 2. Cluster properties of ENSA ensemble.

Cluster	No. of conformers	Cα-Cα RMSD (Å)
100 ENSA conformers		
1	15	19.7
2	10	20.7
3	10	18.5
4	15	21.7
5	7	20.4
6	8	19.4
7	5	18.6
8	3	21.5
9	3	17.1
10	4	15.3
11	2	22.3
12	2	19.6
13	2	18.8
14	5	17.5
15	2	17.3
16	3	17.1
17	1	0
18	1	0
19	1	0
20	1	0
Total	100	–

Table. 3. The EOM analysis of the SAXS data of ENSA. The R_g and D_{max} values obtained from EOM calculation are comparable with those obtained from the primary data processing. Default parameters, 10 000 models in the initial ensemble.

	ENSA^a
EOM^b	
s range for fitting (nm^{-1})	0.10–2.61
Type of models generated	random coil
X^2, *CORMAP P*-value	0.862, 0.811
Constant subtracted	0.006
No. of representative structures	8
R_{flex} (random)/R_{sigma}	77.84% (82.98%) /0.79
Final ensemble R_g/D_{max} (nm)	3.3/10.9

[a]Experimental scattering data from 7 mg·mL^{-1} used.; [b]https://www.embl-hamburg.de/biosaxs/atsas-online/eom.php [46,47].

ENSA, as well as its interaction with PP2A A- and B56-subunits. Our NMR data indicate three regions that have propensity to form transient α-helical structures. All of the three transient helices are involved in PP2A A-subunit binding, forming two binding motifs. The present work provides a better understanding of the structural properties of ENSA and its mode of interaction with PP2A A-subunit. This information can be further utilized, for example in the development of novel and better therapeutics towards PP2A-linked cancer types.

Materials and methods

Recombinant proteins

Human ENSA (UniProt accession number: O43768-1) was cloned to pGTvL1-SGC vector (Structural Genomics Consortium, University of Oxford) using the ligation-independent cloning method [40]. The mutations S67E and S109E were introduced to expression construct using QuikChange II Site-Directed Mutagenesis Kit (Agilent technologies, Santa Clara, CA, USA). All the expression plasmids of ENSA were verified by sequencing. *E.* coli (*Escherichia coli*) BL21gold cells were used for protein production in Terrific Broth (2.4% w/v yeast extract, 1.2% w/v tryptone, 0.5% w/v glycerol, 17 mM KH_2PO_4, 72 mM K_2HPO_4) by the addition of isopropyl-β-D-1-thiogalactopyranoside to 0.4 mM at 18 °C for 20 h. Cells

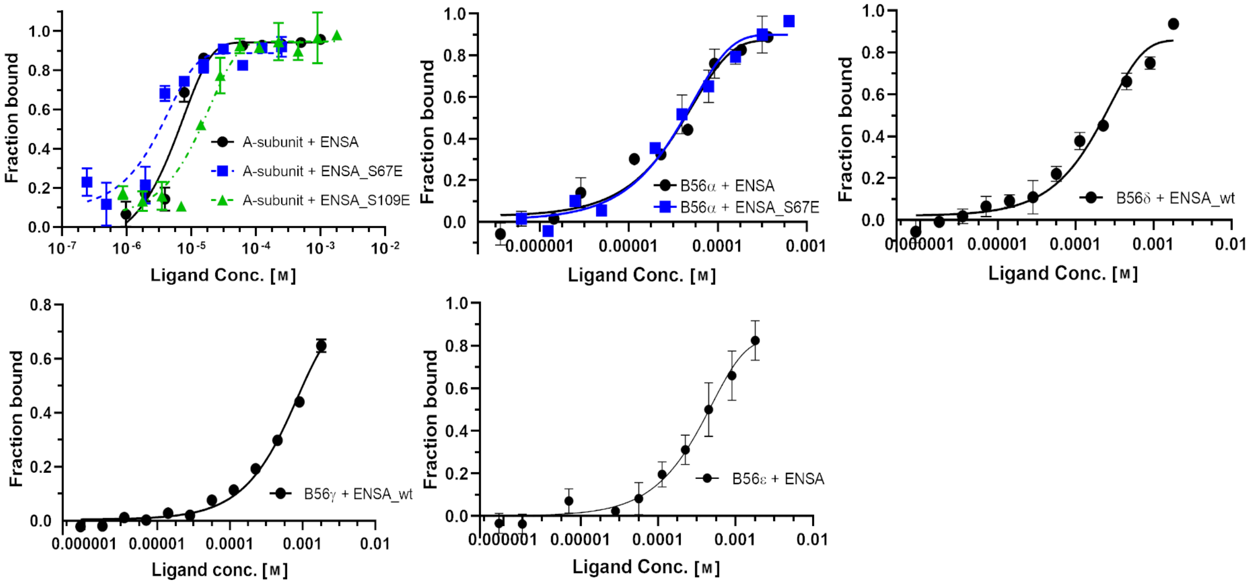

Fig. 8. α-endosulfine interacts stronger to PP2A A-subunit that the B56-subunit. The binding curves obtained from MST experiments show that both ENSA proteins interact with modest affinity to the scaffolding A-subunit. The interaction between ENSA WT and phosphomimicking mutants with the A-subunit is similar. The ENSA WT interacts with different B56-subunits with weak affinity. All phosphomimicking mutants except ENSA S67E failed to bind to B56-subunits which interacts with B56α. MST measurements were performed using fluorescent labelled A- or B56-subunit as a target and unlabelled ENSA as a ligand. The data points represent mean of triplicate (*n* = *3)* data sets and error bars represent standard error of mean (SEM) calculated using GRAPHPAD PRISM version 7.0 for Windows (GraphPad Software Inc).

Table. 4. The equilibrium dissociation constant of ENSA-PP2A A- and B56-subunits interaction determined using MST.

PP2A subunit	ENSA	K_d ± SEM (μM)
A-subunit	WT	3.9 ± 1.3
	S67E	2.5 ± 1.1
	S109E	10.8 ± 3.2
B56α	WT	55.1 ± 27.4
	S67E	32.1 ± 8.1
	S109E	No binding
B56δ	WT	> 137
	S67E	No binding
	S109E	No binding
B56γ	WT	> 250
	S67E	No binding
	S109E	No binding
B56ε	WT	> 460
	S67E	No binding
	S109E	No binding

were lysed to homogeneity using EmulsiFlex-C3 homogenizer (Avestin, Ottawa, ON, Canada) and subsequently centrifuged at 35 000 ***g*** for 30 min at 4 °C to clear the lysate. The GST fusion protein was captured using Protino Glutathione Agarose 4B (Macherey-Nagel, Düren, Germany), and the GST was cleaved by tobacco etch virus (TEV) protease (Invitrogen, Life Technologies, Carlsbad, CA, USA) at 4 °C for 16 h. The TEV protease cleavage extended ENSA constructs by one amino acid residue, S, in N-terminal. HiLoad 26/60 Superdex 200 pg column (GE Healthcare, Chicago, IL, USA) was used for size-exclusion chromatography (SEC) of desired expression construct in SEC buffer (50 mM NaH_2PO_4, pH 6.8, 100 mM KCl, 1 mM DTT) using an ÄKTA pure chromatography system (GE Healthcare). Purified proteins were concentrated using Amicon ultracentrifugal 3K filter device (MilliporeSigma, Burlington, MA, USA). The homodispersity of the proteins was verified with SDS/PAGE.

Fig. 9. α-endosulfine binds to PP2A A-subunit using all preformed transient α-helices. HSQC spectra of ^{15}N-labelled ENSA collected before and after the addition of the PP2A A-subunit indicates that the A-subunit interacts with ENSA. The superposition of ^{15}N-HSQC of ^{15}N-labelled free ENSA (orange) and (A) 1 : 0.5 (cyan), (B) 1 : 1 (grey) and (C) 1 : 2 (maroon) ENSA : PP2A A-subunit. The cross peaks that broadened beyond detection are labelled red, whereas the cross peaks that broadened significantly and shifted the most are labelled magenta and the cross peaks with small changes in intensity and position are labelled blue. (D) ENSA sequence showing the secondary structure elements obtained from SSP calculation and the regions that interacts with the A-subunit of PP2A. The binding regions are colour-coded orange and indicated by B1 and B2.

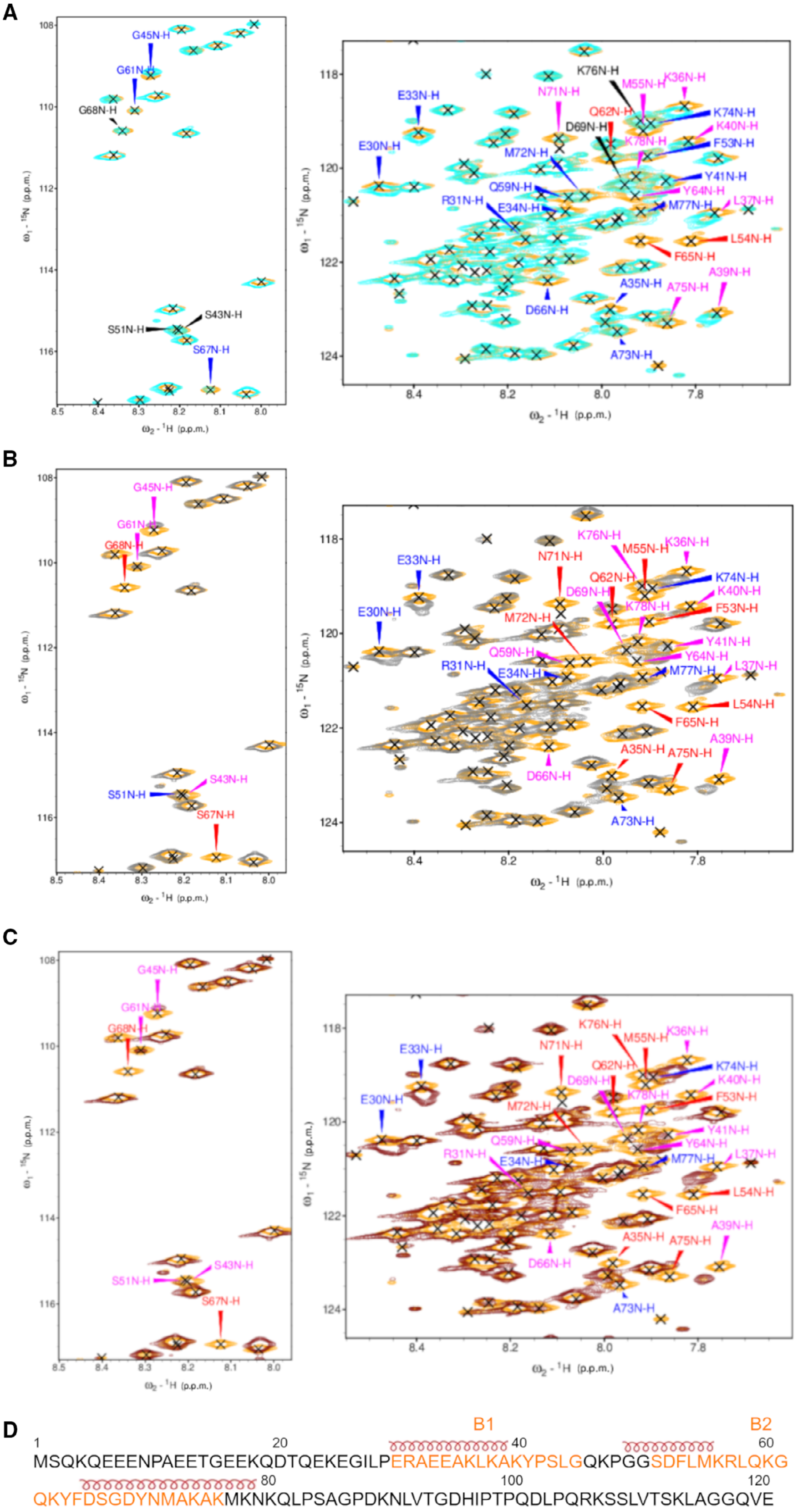
A
B
C
D
G45N-H
G61N-H
G68N-H
S43N-H
S51N-H
S67N-H
E33N-H
E30N-H
R31N-H
E34N-H
K36N-H
L37N-H
A39N-H
K40N-H
Y41N-H
F53N-H
L54N-H
M55N-H
Q59N-H
Q62N-H
Y64N-H
F65N-H
D66N-H
D69N-H
N71N-H
M72N-H
A73N-H
K74N-H
A35N-H
A75N-H
K76N-H
M77N-H
K78N-H
ω1 - 15N (p.p.m.)
ω2 - 1H (p.p.m.)
108
110
112
114
116
118
120
122
124
8.5
8.4
8.3
8.2
8.1
8.0
7.8
B1
B2
1
20
40
60
80
100
120
MSQKQEEENPAEETGEEKQDTQEKEGILPERAEEAKLKAKYPSLGQKPGGSDFLMKRLQKG
QKYFDSGDYNMAKAKMKNKQLPSAGPDKNLVTGDHIPTPQDLPQRKSSLVTSKLAGGQVE

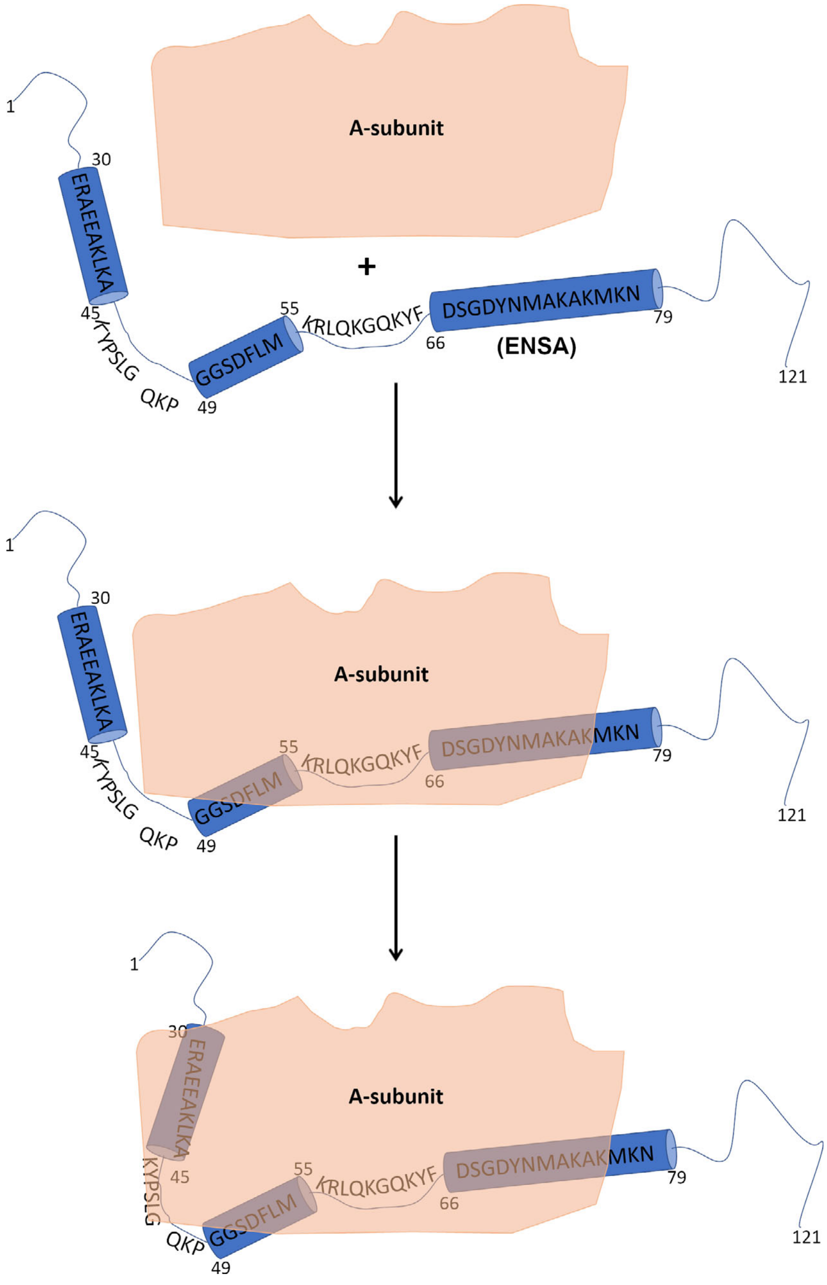

Fig. 10. The schematic diagram of ENSA binding to PP2A A-subunit. According to the NMR titration experiments, ENSA binds to PP2A A-subunit using two-step mechanism. In the first step, a segment comprising second and third transient helix binds to A-subunit. In the subsequent step, a segment comprising first transient helix associates with PP2A A-subunit.

The expression of ^{15}N- and ^{13}C-labelled ENSA constructs was done in *E. coli* BL21 Gold cells in standard M9 minimal medium supplemented with 1 g·L^{-1} ^{15}N NH_4Cl and 2 g·L^{-1} ^{13}C D-glucose as a sole nitrogen and carbon sources, respectively. Protein purification was carried out using the same protocol as described above for the unlabelled proteins in 50 mM NaH_2PO_4, 100 mM NaCl, 1 mM DTT. Protein samples were supplemented with 5% D_2O prior to the NMR measurements.

Small-angle X-ray scattering

European Synchrotron Radiation Facility (ESRF) BM29 [41] beamline at Grenoble, France, was used for SAXS data collection on a Pilatus 1 M image plate using sample detector distance of 2.85 m and wavelength of 0.10 Å, covering the momentum transfer $0.01 < q > 5$ nm^{-1}, where $q = 4\pi \sin(\theta)/\lambda$, and 2θ is scattering angle). Data acquisition was performed with the protein concentrations ranging from 1 to 12.5 mg·mL^{-1}. Gel filtration buffer used in protein dilution was supplemented with 10 mM fresh DTT. The ATSAS program package [42] was used for data processing. The estimation of the radius of gyration (R_g) and maximal dimensions (D_{max}) of the particles were obtained from Guinier analysis performed using PRIMUS [43], and distance distribution functions were calculated using DATGNOM [44]. The flexibility of ENSA was accessed using Kratky plot $(I_{(s)}*s^2$ versus $s)$ [45] and EOM [46,47] on ATSAS online. To ensure the quality of the selected ensemble, CRYSOL [48] was used to compute a simulated scattering curve of all the conformers of the ensemble and it was fitted with the experimental SAXS scattering curve. CRYSOL was run on ATSAS online using default setting. The SAXS profile was back-calculated for individual conformers and averaged, which was then fitted to the experimental data.

Microscale thermophoreis

Microscale thermophoreis experiments were conducted on a Monolith NT. Automated (MA-039) system (NanoTemper Technologies). In all the experiments, PP2A subunits A-subunit, B56α, B56δ, B56γ and B56ε were labelled using Monolith NT Protein labelling kit red NHS, NT-647-NHS fluorescent dye (Cat no. L001, NanoTemper Technologies). The final concentration of PP2A subunits in the experiments was 20 nM in SEC buffer having 0.05% Tween-20. A twofold dilution series of unlabelled ENSA and its phosphomimicking mutants were mixed with labelled proteins. The final concentration of ENSA and its phosphomimicking mutants range from 1.8 mM to 0.2 µM. The experiments were conducted in triplicate. The dissociation constant was calculated using a single-site model to fit the curve using GRAPHPAD PRISM version 8 for Windows (GraphPad Software Inc., La Jolla, CA).

NMR data collection and processing

NMR samples were prepared in 50 mM NaH_2PO_4, 100 mM KCl and 1 mM DTT buffer at pH 6.5. Bruker Avance III HD 800 MHz NMR spectrometer equipped with a Bruker Ascend 18.8 T standard bore magnet, 5 mm triple-resonance inverse TCI CryoProbe (TCI ^1H-$^{13}C/^{15}N$-^2H + Z gradient), was used for data acquisition. All experiments were conducted at 25 °C. For the assignment of backbone chemical shifts, following double- and triple-resonance experiments were performed: 2D ^{15}N-HSQC [28], ^{13}C-CON [29], 3D CBCA(CO)NH, HNCACB [30], iHNCO [32], HNCO [31], iHA(CA)NCO, HA(CA)CON [33] and HA (CA)CON(CA)HA [34]. The steady-state $\{^1H\}$-^{15}N heteronuclear NOEs and ^{15}N R_1 and R_2 relaxation times were measured using the standard relaxation experiments [49]. Time delays for ^{15}N R_1 and R_2 relaxation time were 20, 100, 200, 300, 400, 600, 800, 1000, 1200 and 1400 ms, and 16.96, 67.84, 135.68, 169.6, 203.52, 271.36, 339.2, 407.04, 474.88 and 542.72 ms, respectively. Heteronuclear $\{^1H\}$-^{15}N NOE was measured with 10 s mixing time with and without ^1H saturation. Spectra were processed using TOPSPIN 3.2 software package (Bruker corporation) and analysed using NMRFAM-Sparky 3.13 [50].

Using the SSP software [35], the SSP score was calculated using $^{13}C\alpha$, $^{13}C\beta$ and $^1H\alpha$ chemical shifts of ENSA. The ensemble of structures of ENSA were calculated using ENSEMBLE software suite [51]. The ENSEMBLE tool facilitates the incorporation of different types of data (modules), primarily NMR observables like chemical shifts, ^{15}N R_2 relaxation rate, paramagnetic relaxation enhancement (PRE), NOE and residual dipolar coupling (RDC), and SAXS experimental data into the same refinement protocol and derive ensemble of IDPs. The ENSEMBLE program uses the following three steps to determine the ensemble of structures of IDPs: (a) generation of large set of structures using TraDES (initial soup, 5000) [52,53], (b) random selection of 100 conformers from the initial soup, known as initial pool, and back-calculation of different parameters like NMR chemical shifts, ^{15}N R_2 relaxation rate and SAXS scattering profile of the individual conformers of the initial pool and (c) selection of ensemble of conformers (100 conformers) that best fits the experimental data with the one back-calculated. The chemical shifts of ENSA have been deposited to the BioMagResBank database (http://www.bmrb.wisc.edu) under the accession number 50542.

To ensure the quality of the data, the chemical shift values of the backbone atoms of the conformers in the ensemble were calculated using ShiftX [54] and compared with the experimental data. The input file used for the chemical shift back-calculation was the pdb file containing all the conformers of the ensemble.

^{15}N-HSQC titration by NMR

The PP2A A-subunit titration was performed by adding increasing amount of PP2A A-subunit to ^{15}N-labelled ENSA. The proportion of ENSA and A-subunit of PP2A (ENSA: PP2A A-subunit) used for the titration experiments were 1 : 0.5, 1 : 1 and 1 : 2. All proteins were purified in 20 mM NaH_2PO_4, 50 mM NaCl, 1 mM DTT, pH 6.5. ^{15}N-HSQC titration experiments were performed on a Bruker Avance III HD 800 MHz NMR spectrometer at 25 °C. All spectra were processed with TOPSPIN 3.5 software package (Bruker corporation) and analysed using NMRFAM-Sparky 3.13 [50].

Acknowledgements

We thank ESRF for providing beamline (BM29) access. This work was supported by Academy of Finland [283481 to UP, and 288235 to PP] and the University of Jyväskylä Graduate School [CT.].

Conflict of interest

The authors declare no competing interests.

Author contributions

CT, TH and PR: cloning and protein purification. CT and PP: NMR data collection and analysis. CT, TH and UP: SAXS data collection and analysis. CT, PR and UP: MST data collection and analysis. CT, PP and UP: manuscript preparation.

Peer Review

The peer review history for this article is available at https://publons.com/publon/10.1111/febs.16150.

Data Availability Statement

The chemical shifts of ENSA have been deposited to the BioMagResBank database (http://www.bmrb.wisc.edu) under the accession number 50542.

References

1 Peyrollier K, Heron L, Virsolvy-Vergine A, Le Cam A & Bataille D (1996) A endosulfine is a novel molecule, structually related to a family of phosphoproteins. *Biochem Biophys Res Commun* **223**, 583–586.

2 Heron L, Virsolvy A, Peyrollier K, Gribble FM, Le Cam A, Ashcroft FM & Bataille D (1998) Human α-endosulfine, a possible regulator of sulfonylurea-sensitive KATP channel: molecular cloning, expression and biological properties. *Proc Natl Acad Sci USA* **95**, 8387–8391.

3 Kim SH & Lubec G (2001) Brain α-endosulfine is manifold decreased in brains from patients with Alzheimer's disease: a tentative marker and drug target? *Neurosci Lett* **310**, 77–80.

4 Inagaki N, Gonoi T, Clement JP, Namba N, Inazawa J, Gonzalez G, Aguilar-Bryan L, Seino S & Bryan J (1995) Reconstitution of I(KATP): an inward rectifier subunit plus the sulfonylurea receptor. *Science* **270**, 1166–1170.

5 Sakura H, Ämmälä C, Smith PA, Gribble FM & Ashcroft FM (1995) Cloning and functional expression of the cDNA encoding a novel ATP-sensitive potassium channel subunit expressed in pancreatic β-cells, brain, heart and skeletal muscle. *FEBS Lett* **377**, 338–344.

6 Virsolvy-vergine A, Leray H, Kuroki SHO, Lupo B, Dufour M & Bataille D (1992) Endosulfine, an endogenous peptidic ligand for the sulfonylurea receptor: purification and partial characterization from ovine brain. *Proc Natl Acad Sci USA* **89**, 6629–6633.

7 Sakuta H (1995) ATP-sensitive potassium channel and hormone/neuropeptide. *Nippon Naibunpi Gakkai zasshi* **71**, 579–586.

8 Kim SH & Lubec G (2001) Decreased alpha-endosulfine, an endogenous regulator of ATP-sensitive potassium channels, in brains from adult down syndrome patients. In Protein Expression in Down Syndrome Brain (Lubec G, ed). Springer, Vienna. https://doi.org/10.1007/978-3-7091-6262-0_1

9 Ysselstein D, Dehay B, Costantino IM, McCabe GP, Frosch MP, George JM, Bezard E & Rochet JC (2017) Endosulfine-alpha inhibits membrane-induced α-synuclein aggregation and protects against α-synuclein neurotoxicity. *Herit Sci* **5**, 1–15.

10 Williams BC, Filter JJ, Blake-Hodek KA, Wadzinski BE, Fuda NJ, Shalloway D & Goldberg ML (2014) Greatwall-phosphorylated Endosulfine is both an inhibitor and a substrate of PP2A-B55 heterotrimers. *Elife* **3**, 1–34.

11 Mazhar S, Taylor SE, Sangodkar J & Narla G (2019) Targeting PP2A in cancer: combination therapies. *Biochim Biophys Acta - Mol Cell Res* **1866**, 51–63.

12 Junttila MR, Puustinen P, Niemelä M, Ahola R, Arnold H, Böttzauw T, Ala-aho R, Nielsen C, Ivaska J, Taya Y *et al.* (2007) CIP2A Inhibits PP2A in human malignancies. *Cell* **130**, 51–62.

13 Li M, Guo H & Damuni Z (1995) Purification and characterization of two potent heat-stable protein inhibitors of protein phosphatase 2A from bovine kidney. *Biochemistry* **34**, 1988–1996.

14 Gharbi-Ayachi A, Labbé J-C, Burgess A, Vigneron S, Strub J-M, Brioudes E, Van-Dorsselaer A, Castro A & Lorca T (2010) The substrate of greatwall kinase, Arpp19, controls mitosi by inhibiting protein phosphatese 2A. *Science (80-)* **330**, 1673–1677.

15 Mochida S, Maslen SL, Skehel M & Hunt T (2010) Greatwall phosphorylates an inhibitor of protein phosphatase 2A that is essential for mitosis. *Science (80-)* **330**, 1670–1673.

16 Haesen D, Sents W, Lemaire K, Hoorne Y & Janssens V (2014) The basic biology of PP2A in hematologic cells and malignancies. *Front Oncol* **4**, 1–11.

17 Kauko O & Westermarck J (2018) Non-genomic mechanisms of protein phosphatase 2A (PP2A) regulation in cancer. *Int J Biochem Cell Biol* **96**, 157–164.

18 Chen Y-L, Chuang W-L, Lee C-H, Hsu C-C, Leu Y-W, Huang TH-M, Hsiao S-H, Kuo M-H, Chu P-Y & Lin P-Y (2013) ENSA expression correlates with attenuated tumor propagation in liver cancer. *Biochem Biophys Res Commun* **442**, 56–61.

19 Jackman M, Lindon C, Niggt EA & Pines J (2003) Active cyclin B1-Cdk1 first appears on centrosomes in prophase. *Nat Cell Biol* **5**, 143–148.

20 Uversky VN (2010) The mysterious unfoldome: structureless, underappreciated, yet vital part of any given proteome. *J Biomed Biotechnol* **2010**, 1–14.

21 Hazy E & Tompa P (2009) Limitations of induced folding in molecular recognition by intrinsically disordered proteins. *ChemPhysChem* **10**, 1415–1419.

22 Uversky VN, Gillespie JR & Fink AL (2000) Why are "natively unfolded" proteins unstructured under physiologic conditions? *Proteins Struct Funct Genet* **41**, 415–427.

23 Romero P, Obradovic Z, Li X, Garner EC, Brown CJ & Dunker AK (2001) Sequence complexity of disordered protein. *Proteins Struct Funct Genet* **42**, 38–48.

24 Mészáros B, Erdös G & Dosztányi Z (2018) IUPred2A: context-dependent prediction of protein disorder as a function of redox state and protein binding. *Nucleic Acids Res* **46**, W329–W337.

25 Erdős G & Dosztányi Z (2020) Analyzing protein disorder with IUPred2A. *Curr Protoc Bioinforma* **70**, e99.

26 Thapa CJ, Haataja T, Pentikäinen U & Permi P (2020) 1H, 13C and 15N NMR chemical shift assignments of cAMP-regulated phosphoprotein-19 and -16 (ARPP-19 and ARPP-16). *Biomol NMR Assign* **14**, 227–231.

27 Thapa C, Roivas P, Haataja T, Permi P, De SA & Gianni S (2021) The interaction mechanism of intrinsically disordered PP2A inhibitor proteins ARPP-16 and ARPP-19 with PP2A. *Front Mol Biosci* **8**, 1–16.

28 Kay LE, Keifer P & Saarinen T (1992) Pure absorption gradient enhanced heteronuclear single quantum correlation spectroscopy with improved sensitivity. *J Am Chem Soc* **114**, 10663–10665.

29 Bermel W, Bertini I, Duma L, Felli IC, Emsley L, Pierattelli R & Vasos PR (2005) Complete assignment of heteronuclear protein resonances by protonless NMR spectroscopy. *Angew Chemie Int Ed* **44**, 3089–3092.

30 Yamazaki T, Muhandiranv DR, Kay LE, Lee W & Arrowsmith CH (1994) A suite of triple resonance NMR experiments for the backbone assignment of 15N, 13C, 2H labeled proteins with high sensitivity. *J Am Chem Soc* **116**, 11655–11666.

31 Kay LE, Xu GY & Yamazaki T (1994) Enhanced-sensitivity triple-resonance spectroscopy. *J Magn Reson* **109**, 129–133.

32 Mäntylahti S, Tossavainen H, Hellman M & Permi P (2009) An intraresidual i(HCA)CO(CA)NH experiment for the assignment of main-chain resonances in 15N, 13C labeled proteins. *J Biomol NMR* **45**, 301–310.

33 Mäntylahti S, Aitio O, Hellman M & Permi P (2010) HA-detected experiments for the backbone assignment of intrinsically disordered proteins. *J Biomol NMR* **47**, 171–181.

34 Mäntylahti S, Hellman M & Permi P (2011) Extension of the HA-detection based approach: (HCA)CON(CA)H and (HCA)NCO(CA)H experiments for the main-chain assignment of intrinsically disordered proteins. *J Biomol NMR* **49**, 99–109.

35 Marsh JA, Singh VK, Jia Z & Forman-Kay JD (2006) Sensitivity of secondary structure propensities to sequence differences between α- and γ-synuclein: implications for fibrillation. *Protein Sci* **15**, 2795–2804.

36 Farrow NA, Zhang O, Szabo A, Torchia DA & Kay LE (1995) Spectral density function mapping using 15N relaxation data exclusively. *J Biomol NMR* **6**, 153–162.

37 Lefevre JF, Dayie KT, Peng JW & Wagner G (1996) Internal mobility in the partially folded DNA binding and dimerization domains of GAL4: NMR analysis of the N-H spectral density functions. *Biochemistry* **35**, 2674–2686.

38 Kelley LA, Gardner SP & Sutcliffe MJ (1996) An automated approach for clustering an ensemble of NMR-derived protein structures into conformationally related subfamilies. *Protein Eng* **9**, 1063–1065.

39 Tompa P & Fuxreiter M (2008) Fuzzy complexes: polymorphism and structural disorder in protein–protein interactions. *Trends Biochem Sci* **33**, 2–8.

40 Savitsky P, Bray J, Cooper CDO, Marsden BD, Mahajan P, Burgess-Brown NA & Gileadi O (2010) High-throughput production of human proteins for crystallization: the SGC experience. *J Struct Biol* **172**, 3–13.

41 Pernot P, Round A, Barrett R, De Maria AA, Gobbo A, Gordon E, Huet J, Kieffer J, Lentini M, Mattenet M *et al.* (2013) Upgraded ESRF BM29 beamline for SAXS on macromolecules in solution. *J Synchrotron Radiat* **20**, 660–664.

42 Franke D, Petoukhov MV, Konarev PV, Panjkovich A, Tuukkanen A, Mertens HDT, Kikhney AG, Hajizadeh NR, Franklin JM, Jeffries CM & *et al.* (2017) ATSAS 2.8: a comprehensive data analysis suite for small-angle scattering from macromolecular solutions. *J Appl Crystallogr* **50**, 1212–1225.

43 Konarev PV, Volkov VV, Sokolova AV, Koch MHJ & Svergun DI (2003) PRIMUS : a windows PC-based system for small-angle scattering data analysis. *J Appl Crystallogr* **36**, 1277–1282.

44 Petoukhov MV, Konarev PV, Kikhney AG & Svergun DI (2007) ATSAS 2.1 - towards automated and web-supported small-angle scattering data analysis. *J Appl Crystallogr* **40**, 223–228.

45 Durand D, Vivès C, Cannella D, Pérez J, Pebay-Peyroula E, Vachette P & Fieschi F (2010) NADPH oxidase activator p67phox behaves in solution as a multidomain protein with semi-flexible linkers. *J Struct Biol* **169**, 45–53.

46 Bernadó P, Mylonas E, Petoukhov MV, Blackledge M & Svergun DI (2007) Structural characterization of flexible proteins using small-angle X-ray scattering. *J Am Chem Soc* **129**, 5656–5664.

47 Tria G, Mertens HDT, Kachala M & Svergun DI (2015) Advanced ensemble modelling of flexible macromolecules using X-ray solution scattering. *IUCrJ* **2**, 207–217.

48 Svergun D, Barberato C & Koch MHJ (1995) CRYSOL – a program to evaluate X-ray solution scattering of biological macromolecules from atomic coordinates. *J Appl Crystallogr* **28**, 768–773.

49 Farrow NA, Muhandiram R, Singer AU, Pascal SM, Kay CM, Gish G, Shoelson SE, Pawson T, Forman-Kay JD & Kay LE (1994) Backbone dynamics of a free and a phosphopeptide-complexed Src homology 2 domain studied by 15N NMR relaxation. *Biochemistry* **33**, 5984–6003.

50 Lee W, Tonelli M & Markley JL (2014) NMRFAM-SPARKY: enhanced software for biomolecular NMR spectroscopy. *Bioinformatics* **31**, 1325–1327.

51 Krzeminski M, Marsh JA, Neale C, Choy WY & Forman-Kay JD (2013) Characterization of disordered proteins with ENSEMBLE. *Bioinformatics* **29**, 398–399.

52 Feldman HJ & Hogue CWV (2000) A fast method to sample real protein conformational space. *Proteins Struct Funct Genet* **39**, 112–131.

53 Feldman HJ & Hogue CWV (2002) Probabilistic sampling of protein conformations: new hope for brute force? *Proteins Struct Funct Genet* **46**, 8–23.

54 Neal S, Nip AM, Zhang H & Wishart DS (2003) Rapid and accurate calculation of protein 1H, 13C and 15N chemical shifts. *J Biomol NMR* **26**, 215–240.

55 Pettersen EF, Goddard TD, Huang CC, Meng EC, Couch GS, Croll TI, Morris JH & Ferrin TE (2021) UCSF ChimeraX: structure visualization for researchers, educators, and developers. *Protein Sci* **30**, 70–82.